aerospace

MDPI

Article

Efficient High-Precision Measurement for Micro-Orifice Parameters of Impinging Injectors

Haitao Li *, Yunhong Bai, Yawen Wang, Mengyang Zhang, Yikang Zhang, Lijun Yang, Chi Ma and Jie Li

School of Mechanical and Electrical Engineering, Shaanxi University of Science and Technology, Xi'an 710021, China; 240512133@sust.edu.cn (M.Z.)

* Correspondence: lihaitao@sust.edu.cn; Tel.: +86-153-8944-8983

Abstract

Impinging injectors are extensively utilized in liquid rocket engines, characterized by a large number of paired inclined injection orifices. The diameter and axis alignment deviation of these orifices directly influence propellant flow distribution, atomization and mixing behavior, and engine operational stability. To address the challenges associated with micro-sized orifices, inclined axes, large quantities, spatial intersection, and the low detection efficiency of conventional approaches, this paper proposes a dual-line laser 3D point cloud reconstruction-based method for measuring the diameter and impact alignment deviation of injector orifices. A dual-line laser measurement system is established to capture surface point clouds on both sides of the orifice inlets. Through system calibration and point cloud registration, the 3D point cloud data of the injector orifices within a unified coordinate system are reconstructed. Cross-sectional mapping, boundary extraction, and geometric fitting techniques are applied to determine the diameter and axis parameters of the orifices, and the spatial alignment deviation of paired orifices is subsequently calculated. To validate the feasibility of the proposed method, experimental investigation is conducted on test specimens with both 8 pairs of Φ2 mm through-holes and Φ0.5 mm micro-orifices. For the Φ2 mm specimen, the diameter measurement results are compared with industrial computed tomography (CT) data, while the alignment deviation results are verified using a combination of pin gauges and coordinate measuring machine (CMM) measurements. For the Φ0.5 mm micro-orifices, both diameter and alignment deviation results are verified using a 3D coaxial line confocal sensor. After system calibration, the fitting residuals of three Φ8 mm standard spheres are all maintained within 0.08 mm. The diameter measurement results of 8 selected Φ2 mm orifices show good overall agreement with industrial CT data: the maximum absolute deviation is 22 μm, the average absolute deviation is 15 μm, the maximum relative error is 1.09%, and the average relative error is 0.74%. The diameter and alignment deviation results of Φ0.5 mm micro-orifices show good consistency with the 3D coaxial line confocal sensor: the maximum absolute deviation is 13 μm for diameter and 0.047° for alignment deviation, with maximum relative errors of 2.41% and 0.058%, respectively. The alignment deviation results of 8 pairs of Φ2 mm orifices indicate that the proposed dual-line laser method is generally consistent with the combined pin gauge and CMM approach: the maximum absolute deviation is 0.170°, the average absolute deviation is 0.125%, the maximum relative error is 0.284%, and the average relative error is 0.125%. The results demonstrate that the proposed method enables non-contact and high-efficiency measurement of the diameter and alignment angle of injector orifices in impinging injectors for both conventional Φ2 mm orifices and micro Φ0.5 mm orifices, with high measurement accuracy and promising engineering application potential, thereby providing a new technical approach for the geometric parameter inspection of multi-scale micro-injection orifices.

Check for updates

Academic Editor: Kyun Ho Lee

Received: 17 April 2026
Revised: 16 May 2026
Accepted: 18 May 2026
Published: 22 May 2026

Copyright: © 2026 by the authors. Licensee MDPI, Basel, Switzerland. This article is an open access article distributed under the terms and conditions of the Creative Commons Attribution (CC BY) license.

Keywords: impinging injectors; line laser; micro-orifice; diameter measurement; impact alignment deviation

1. Introduction

Impinging injectors are essential components for propellant supply and atomization-mixing in liquid rocket attitude and orbit control engines [1]. The manufacturing quality of their injection orifices directly affects the stability and atomization efficiency of the propellant injection process [2]. For paired injection orifices, the orifice diameter determines the regulation accuracy of propellant injection flow rate, while the alignment deviation controls the spatial impingement condition of the two jets, further affecting propellant atomization performance [3–5]. Therefore, the injection orifice diameter and alignment deviation are regarded as key parameters for evaluating the manufacturing quality and injection performance of orifices [6,7], and they are of considerable importance for the operational reliability and on-orbit performance of attitude and orbit control engines.

At present, the machining accuracy of injection orifices is mainly guaranteed through the optimization of processing techniques, while a complete and systematic inspection method and system have not yet been fully developed. The main challenges can be summarized as follows: (1) micro-scale orifice diameters, typically ranging from Φ0.2 mm to Φ2 mm, which impose strict limitations on sensor size for probe-based intrusive measurement methods; (2) a large number of orifices, with hundreds of pairs of micro-orifices requiring inspection, resulting in low efficiency when measured individually; (3) a compact spatial arrangement, where the central axes are obliquely distributed, leading to significant interference when sensors are positioned at inclined angles; (4) the spatial impingement point represents a virtual feature that cannot be directly detected by physical sensors; (5) fixed-diameter characteristics, meaning different orifice sizes require different contact sensors or gauges, thereby increasing measurement complexity and cost.

Existing measurement techniques for injection orifices mainly include contact and non-contact approaches. Contact measurement methods generally rely on coordinate measuring machines, micro-probes, pin gauges, and similar tools to evaluate orifice diameters and axis-related parameters. Due to their relatively high measurement accuracy, such methods have been applied to some extent in the inspection of hole structures [8]. Non-contact measurement methods mainly include vision measurement, industrial CT, laser scanning, and related techniques [9,10], which offer advantages such as avoiding contact-induced damage, high sampling efficiency, and a high degree of automation [11,12]. Among these, vision measuring instruments can conveniently obtain the orifice contour and two-dimensional information, making them suitable for measuring parameters such as orifice diameter [13–15]. Laser scanning methods can acquire three-dimensional point cloud data of the measured surface, thereby providing data support for the evaluation of complex structural parameters [16,17]. Therefore, existing studies have established two main technical routes for orifice size measurement: contact and non-contact. However, considering the structural characteristics of impinging injector orifices, including small diameter, large quantity, complex inclined axis distribution, and paired orifice staggering, measurement equipment and methods are required to achieve both high precision and high efficiency simultaneously. Existing methods still exhibit evident limitations, and no mature measuring equipment or methods have been widely adopted in engineering practice. Pin gauges are fixed-size measuring tools that require repeated fitting attempts for different orifice sizes and can easily damage the inner wall. Micro-probes exhibit extremely unstable manufacturability and incur high cost. Thus, although contact methods provide high accu-

racy, they face issues such as limited probe size, low efficiency in sequential single-orifice inspection, and complicated implementation when measuring micro-injection orifices [18]. Among non-contact methods, vision measuring instruments and similar devices mainly obtain information based on two-dimensional imaging or projected contours, which requires light to pass through micro-orifices. They can be applied for diameter measurement when the normal direction of the orifice centerline is perpendicular to the image plane; however, it remains difficult to accurately characterize the spatial orientation of orifice axes and the spatial relationship between paired orifices, making the measurement of alignment deviation challenging. Industrial CT can obtain internal structural data, but its measurement accuracy is highly dependent on the volume of the measured part, while its measurement efficiency and data processing speed are relatively low, and radiation is also involved [19]. To overcome the above limitations, this paper proposes a measurement method for orifice diameter and alignment deviation based on dual-line laser scanning. Bilateral line lasers are employed to synchronously acquire point cloud data of the contours on both sides and within the injection orifices. A point cloud reconstruction and parameter solution model under a unified coordinate system is developed. Through non-contact double-sided scanning, direct measurement of orifice diameter and indirect estimation of alignment deviation are achieved. Therefore, the proposed method satisfies the requirements of both high precision and high efficiency.

2. Establishment of the Measurement System

2.1. Measurement Object and Principle

2.1.1. Measurement Object

Figure 1 presents a schematic diagram of the injector orifices. Paired micro inclined holes are fabricated on the nozzle, and the parameters to be measured include the diameter of the micro inclined holes and their impingement accuracy. The red dashed lines in the figure represent the central axes of the paired injection orifices.

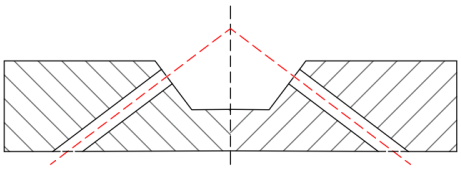


Figure 1. Schematic diagram of paired injection orifice structure.

Impingement accuracy represents the spatial alignment deviation between the axes of paired injection orifices. Figure 2 illustrates a schematic diagram of the spatial misalignment. In this figure, the blue and red rods represent the axes of the paired injection orifices, while the dashed lines and arrows in the inset indicate the spatial intersection error and its direction.

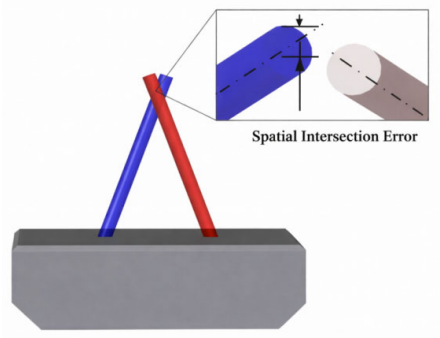


Figure 2. Schematic diagram of alignment deviation.

2.1.2. Measurement Principle

As illustrated in Figure 3a, a line laser sensor functions based on the principle of laser triangulation. A uniform laser line is projected onto the surface of the measured object by a laser emitter, and the reflected laser signal is captured by a high-resolution sensor. By evaluating the positional variation in the reflection point on the receiver and incorporating the geometric parameters of the sensor, the height and spatial position of the object surface can be accurately determined. Through controlled motion of either the sensor or the measured object, multiple two-dimensional profile datasets are sequentially acquired and finally integrated into a complete three-dimensional point cloud. A single line laser sensor enables high-precision acquisition of surface point cloud data. As shown in Figure 3b, two line laser sensors are arranged oppositely on both sides of the measured hole, allowing point cloud data to be obtained from both sides of the micro-orifice.

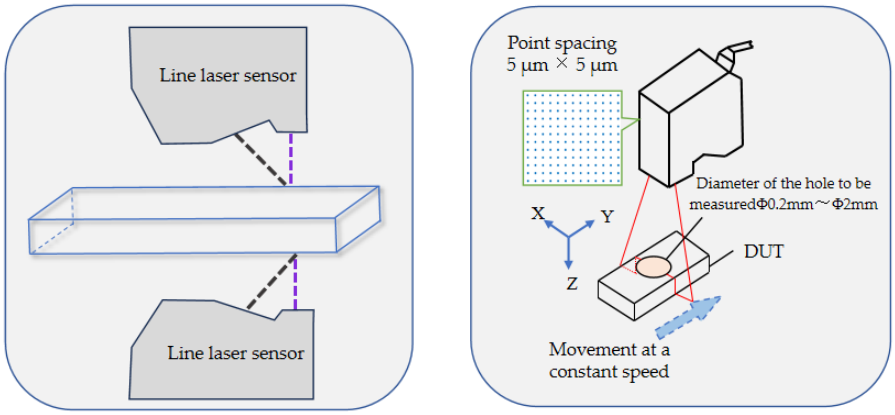


Figure 3. Measurement principle of micro-orifices: (**a**) Front View; (**b**) Top View.

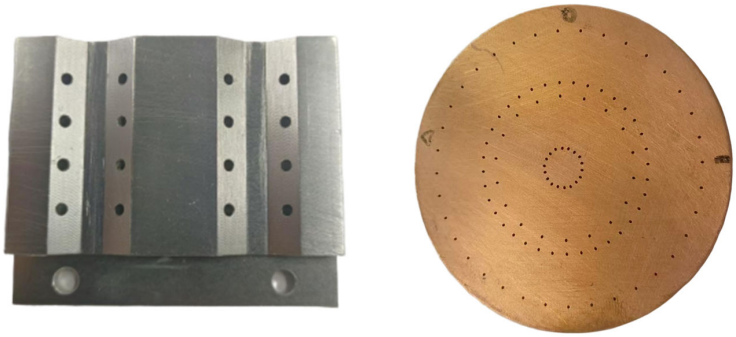
Due to the small diameter of the injection orifices, the point density must significantly exceed the orifice size to fully reconstruct the hole edge profile and enhance the accuracy of small-hole fitting. The data point interval of line laser sensors typically reaches 3–5 μm. As illustrated in Figure 3, the measurement interval is considerably smaller than the orifice scale, which is sufficient to capture detailed edge features of micro-orifices. Even for micro-orifices with a diameter of Φ1 mm, more than 200 rows of measurement data can be collected, thereby ensuring measurement accuracy and completeness. Due to the inclination of the orifice, line-of-sight occlusion occurs in single-side measurement: no valid data can be obtained from one side of the orifice entrance, while point cloud information of a certain depth of the inner wall can be collected from the other side. This system adopts synchronous scanning by bilateral line lasers, and uses combined fitting of bilateral orifice entrance profile data and bilateral orifice inner wall local data to solve the problem of data loss caused by inclination occlusion, ensuring the stable solution of cylindrical geometric parameters of micro-orifices. In addition, insufficient displacement measurement accuracy leads to accumulated registration errors and reduces the integrity and accuracy of the overall dataset. Therefore, a high-precision linear module is employed to drive the measured part or the line laser sensors at a constant velocity, ensuring the stability of point cloud data during the acquisition process.

After acquiring the point cloud data from both sides of the measured orifice, the datasets collected by the two sensors are registered and further processed. The average value of the orifice diameters fitted from the point clouds on both sides is taken as the final measured aperture value. The spatial axis of each injection orifice is determined using

the center coordinates obtained from both sides, and the spatial misalignment error of the paired injection orifices, namely the impingement accuracy, is subsequently calculated.

2.2. Test Specimen Fabrication

In engineering practice, the diameter of injection orifices typically ranges from Φ0.2 mm to Φ2 mm. Considering the machining limitation, ultra-small Φ0.2 mm orifices are prone to burrs and poor forming quality. For better comparison and validation, two types of orifices (Φ0.5 mm and Φ2 mm) are machined. The theoretical impingement angle is designed as 60° for Φ2 mm orifices in Figure 4a and 80° for Φ0.5 mm orifices in Figure 4b, respectively.



(**a**) (**b**)

Figure 4. Injection orifice test specimen: (**a**) Φ2 mm hole; (**b**) Φ0.5 mm hole.

2.3. Measurement System Setup

As illustrated in Figure 5, the developed dual-line laser measurement system for injection orifices mainly consists of two line laser sensors, a sensor mounting bracket, a precision linear module, a three-axis fine-tuning device, and a sample fixture.

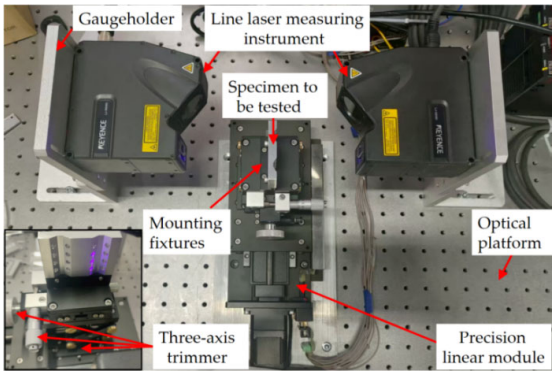


Figure 5. Line laser measurement system for injection orifices.

Two line laser sensors are mounted on an optical platform via a sensor bracket. Waist slots are machined on the bracket to enable adjustment of the relative positions of the sensors. The precision linear module is installed on the optical platform through a connecting plate, and a three-axis fine-tuning device is mounted on the sliding table to accurately position the test specimen within the effective measurement range of the two sensors. The specimen is secured on the three-axis fine-tuning device using a fixture, and the micro-orifices on the specimen are inclined within the sensor coordinate system. During bracket installation, a dial indicator is utilized to finely adjust the bracket position to ensure parallelism with the motion direction of the module, which facilitates subsequent system calibration and data acquisition.

The system adopts the LJ-X8060 3D line laser sensor produced by Keyence Corporation (Osaka, Japan), with repeatability accuracies of 0.4 μm and 0.5 μm in the X and Z axes, respectively, and a point interval of 5 μm for the acquired point cloud data. The repeat positioning accuracy of the precision linear module is ±0.5 μm. Figure 6 presents the wiring diagram of the system. A Siemens S7-200 Smart series PLC is employed as the controller to precisely regulate the stepper motor and trigger the line laser sensors, while a switch is responsible for transmitting the data collected by the two line laser sensors.

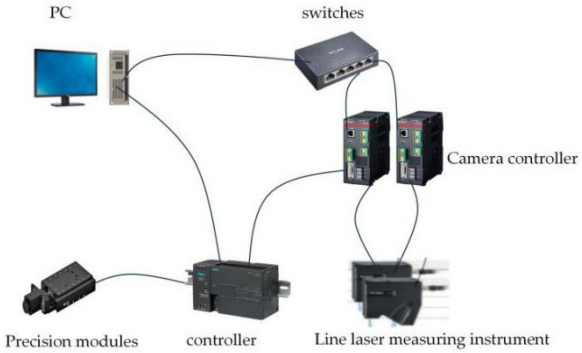


Figure 6. Wiring diagram of the measurement system.

The measurement procedure is as follows: First, the installation poses of the two line laser sensors are calibrated to determine their spatial relative positions. Second, as shown in Figure 7, point cloud data on both sides of the injection orifice are acquired separately, and the two sets of point clouds are accurately registered based on the calibration results. Third, the registered point cloud is fitted to obtain the diameter and center coordinates of the micro-orifice, and the orifice diameter and impingement accuracy are calculated according to the fitting results.

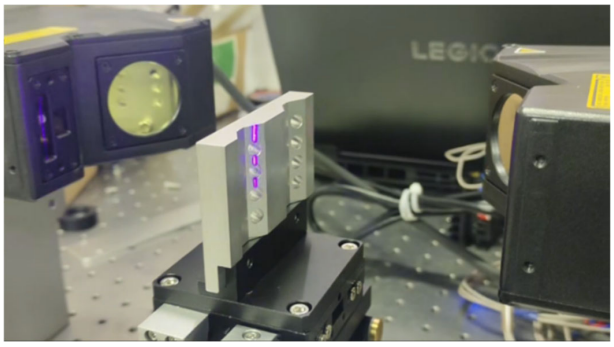


Figure 7. Schematic diagram of the point cloud acquisition process.

3. Calibration and Data Registration of the Measurement System

3.1. Measurement System Calibration

To enhance the measurement accuracy of the injection orifice impingement error, it is necessary to precisely register the point cloud data acquired by the two sensors, so that the center coordinates of the cross-sectional circles on both sides of the micro-orifice can be accurately fitted [20,21]. Therefore, accurate calibration and establishment of the spatial coordinate relationship between the two line laser sensors in the measurement system are particularly essential.

The measuring ranges of the adopted line laser sensor are 16 mm in the *X*-axis and 14.6 mm in the *Z*-axis, respectively. Conventional calibration methods (such as the ICP matching algorithm or machining a dedicated calibration block [22]) are not suitable for this system. Accordingly, this paper proposes a dual-line laser calibration approach based

on a standard sphere. An 8 mm standard sphere is selected as the calibration object, and the left and right hemispheres are scanned by the two line lasers to obtain hemispherical point cloud data. The sphere center is then fitted, and the spatial invariance of the sphere center is utilized to determine the spatial transformation relationship between the two sensor coordinate systems, thereby establishing a unified world coordinate system.

Figure 8 presents a schematic diagram of the standard sphere-based calibration method. First, three non-collinear threaded holes with different heights are designed to mount the calibration sphere, thereby determining its spatial pose in three-dimensional coordinates. Then, by adjusting the three-axis fine-tuning device, the two adjacent surfaces of the calibration sphere are positioned within the measuring ranges of the two sensors, respectively. L_1 and L_2 denote the camera coordinate systems of the two line laser sensors, and the world coordinate system L_0 is defined at the center point of the larger plane on the left side of the standard sphere. The point cloud data collected by the two line laser sensors in their respective coordinate systems are transformed into the world coordinate system, and the transformation matrix is computed, thus completing the calibration of the dual-line laser measurement system. In Figure 8, the colored coordinate axes ($X_1/Y_1/Z_1$, $X_2/Y_2/Z_2$) represent the coordinate systems of the two line laser sensors, and the arrows indicate the direction of each axis. The red axes (L_1, L_2, L_0) represent the world coordinate system defined by the standard calibration sphere.

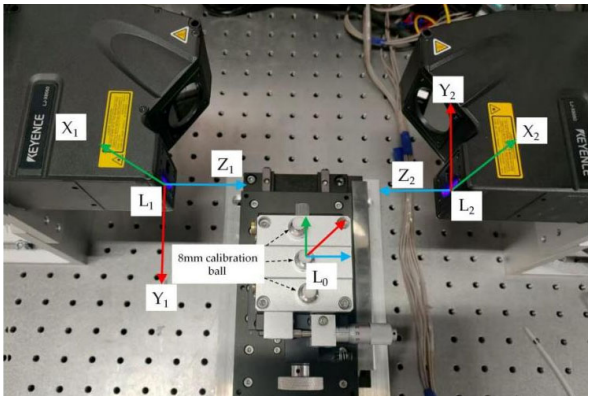


Figure 8. Calibration of the measurement system.

Due to the large volume of the acquired point cloud data, point cloud simplification is first conducted to remove noise and redundant information and to improve computational efficiency. The simplified point cloud result is illustrated in Figure 9.

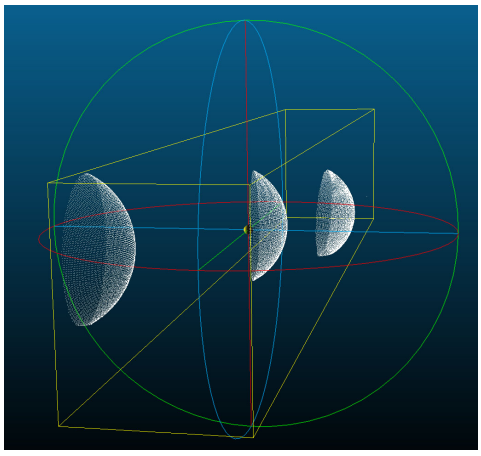


Figure 9. Simplified point cloud.

The proposed point cloud calibration method based on three Φ8 mm standard spheres mainly consists of three steps:

(1) Sphere fitting: First, spherical fitting is performed on the semicircular point clouds of the three calibration spheres in the left and right datasets, respectively, to obtain the center coordinates and radius of each sphere. In this step, the point clouds containing only partial spherical data are converted into complete geometric parameters, providing a reference basis for matching the left and right point clouds.

(2) Sphere center correspondence and rigid transformation calculation: After obtaining the three sphere centers on each side, the Euclidean distances between the two sets of centers are computed, and the correspondence is established using the minimum distance matching principle, which is a fundamental geometric strategy that aligns two point sets by minimizing the Euclidean distance between corresponding points. Then, based on the paired sphere centers, the Kabsch algorithm, a well-established least-squares method for estimating the optimal rigid transformation between two point sets [23], is employed to solve the rigid transformation matrix, yielding the rotation matrix and translation vector from the right coordinate system to the left one. This step effectively unifies the coordinate systems of the two-side point clouds.

(3) Point cloud registration. The derived rigid transformation is applied to the right point cloud and sphere centers to map them into the left coordinate system, which are subsequently merged with the left point cloud to form a complete registered dataset. Meanwhile, the corresponding left and right sphere centers are averaged to obtain the final registered sphere centers and radii. Finally, the accuracy of the calibration method is evaluated by examining the sphere fitting residuals, sphere center registration errors, and the deviation between the fitted radius and the theoretical value.

Through the above three steps, the left and right point cloud data are registered with high precision within a unified coordinate system, thereby completing the calibration from the camera coordinate systems to the world coordinate system.

First, single-sphere point cloud fitting is performed. The single-sphere point cloud set is denoted as:

$$\{P_i = (x_i, y_i, z_i)\}_{i=1}^{N} \tag{1}$$

The geometric equation of the fitted sphere is:

$$x^2 + y^2 + z^2 + ax + by + cz + d = 0 \tag{2}$$

where a, b, c, d denotes the parameters to be estimated, and (x, y, z) represents the coordinates of an arbitrary point in the point cloud. Fit the parameters a, b, c, d using the least squares method. The sphere center and radius were then derived as $(-a/2, -b/2, -c/2)$ and $\sqrt{(a^2 + b^2 + c^2)/4 - d}$.

The sphere parameters were estimated by minimizing the sum of squared residuals using MATLAB R2022b's lsqnonlin function.

In the experiment, three Φ8 mm standard ceramic spheres were used as the calibration reference. The three spheres in the left and right point clouds were independently fitted using the least squares method in MATLAB, as illustrated in Figure 10. The coordinates of the left-view sphere centers obtained are as follows:

$$c_1^L = (4.2404, 48.5771, -3.5352) \tag{3}$$

$$c_2^L = (6.3368, 28.5607, -1.1789) \tag{4}$$

$$c_3^L = (8.2747, 8.6178, 2.7660) \tag{5}$$

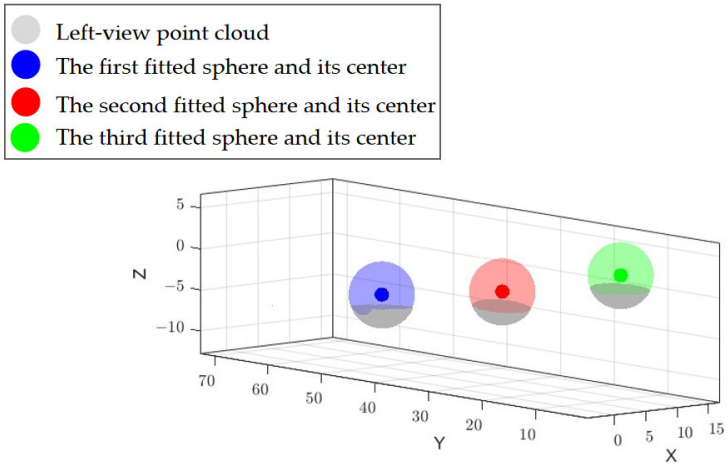


Figure 10. Fitting results of the left hemisphere centers of standard spheres.

Figure 10 shows the fitting result of the calibration sphere. The small semicircular point cloud at the bottom is the valid point cloud obtained by the left line laser sensor after denoising and simplification. After removing a large number of scattered noise points, only the effective local point cloud of the calibration sphere is retained. On the basis of this reserved semicircular point cloud, the complete circular contour is obtained by spherical fitting. The marker in the middle is the sphere center solved from the fitting result. The calibration sphere used is G5-grade high-precision standard ceramic sphere, with a surface roughness Ra $\leq$ 0.025 μm and sphericity error $\leq$ 0.25 μm. The average fitted radius is 3.997 mm, which is highly consistent with the theoretical true radius of 4.000 mm.

The average radius is about 3.98 mm, and the corresponding plane is shown in Figure 11.

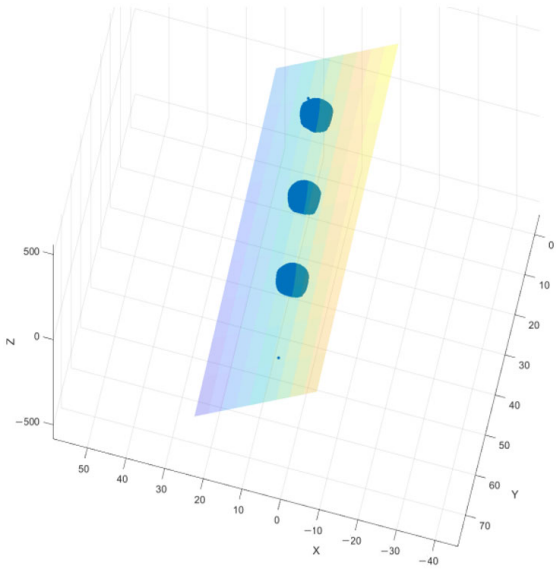


Figure 11. Plane determined by the centers of the left hemispherical standard spheres.

Figure 11 illustrates the spatial reference plane determined by the three non-collinear sphere centers which are all fitted from the denoised effective semicircular point clouds of the left line laser sensor. In this figure, the three blue points represent the centers of the calibrated spheres, and the gradient-colored plane is the fitted spatial reference plane. This plane is established as the calibration reference plane of the dual-line laser measurement system, which constrains the spatial coordinate relationship between the left and right

sensors and provides a reliable reference for subsequent point cloud registration and parameter calculation.

After fitting the left and right point clouds, the coordinate matrix of the three sphere centers is obtained.

To establish the geometric correspondence between the left and right point clouds, the matching order of the three sphere centers must first be determined, and then defined using the Euclidean distance matrix.

Explanation of the matching process:

Because the order of the three sphere centers obtained from the left and right sensors may not match, we first computed the Euclidean distance matrix between the two sets of centers. Using the Hungarian algorithm (implemented via *matchpairs* in *MATLAB*), we found the one-to-one correspondence that minimized the total distance. This permutation step is essential to correctly pair the sphere centers before computing the rigid transformation.

Using this transformation matrix, the right-view point cloud can be transformed into the left-view coordinate system, thereby achieving spatial registration of the two-view data and providing a consistent geometric basis for subsequent point cloud stitching.

The Kabsch algorithm is used to compute the rotation matrix R and translation vector t from the right point cloud to the left coordinate system. For any point X in the right point cloud, its corresponding point in the left coordinate system can be obtained via coordinate transformation.

$$X' = RX + t \tag{6}$$

This inner product equation is retained because it serves as the core geometric foundation for calculating the spatial alignment angle between paired injection orifice axes, which is essential for evaluating the impingement accuracy of the injector.

After stitching the two fields of view, to ensure consistency of the three-sphere fitting results, the sphere centers and radii after fusion are calculated using a weighted averaging strategy:

$$c_i = \frac{1}{2}\left(c_i^L + \left(Rc_{\pi(i)}^R + t\right)\right), r_i = \frac{1}{2}\left(r_i^L + r_{\pi(i)}^R\right), i = 1,2,3 \tag{7}$$

After applying the rigid transformation T to the right-side point cloud P_R, we merged it with the left-side point cloud P_L by simple concatenation:

$$P_{fused} = P_L \cup (T \cdot P_R) \tag{8}$$

P_L and P_R are the original point clouds (sets of 3D points), and T is the 4×4 homogeneous transformation matrix.

Subsequently, the iterative closest point (ICP) algorithm, an iterative optimization technique widely utilized for precise 3D point cloud registration by minimizing the distance between corresponding points in successive iterations [24], is applied for local refinement to further improve the stitching accuracy. The fusion result is shown in Figure 12, where the stitched point cloud exhibits a continuous surface without noticeable misalignment, verifying the correctness and reliability of the derived rigid-body transformation and matching correspondence.

Figure 12 presents the final fitting and registration results of the calibration sphere. The upper and lower hemispheres correspond to the left-view and right-view point clouds obtained by the two sensors. Rigid transformation unifies them into the same coordinate system for accurate alignment. The wavy points are noise caused by laser scanning limitations and have been removed before fitting to ensure calibration accuracy.

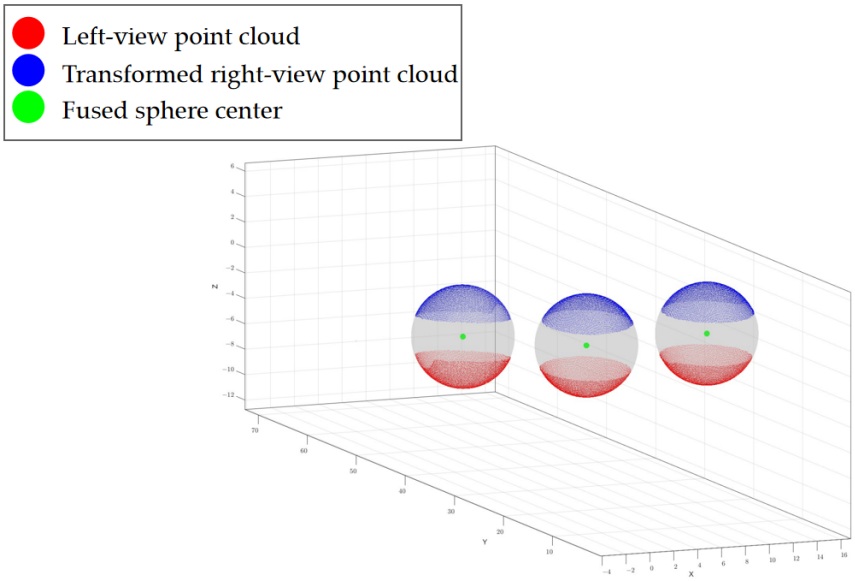


Figure 12. Fitting results of calibration spheres.

3.2. Accuracy Verification

To quantitatively assess the accuracy of calibration sphere fitting and point cloud stitching, the root mean square (*RMS*) error is adopted to measure the deviation between the fitted spherical surface and the point cloud data. *RMS* can effectively reflect the overall average deviation between the point cloud and the fitting model, and is an important indicator for evaluating system calibration accuracy.

Let the coordinates of the fitted sphere center be (x_0, y_0, z_0), the radius be R, and the coordinates of the i-th point in the point cloud be (x_i, y_i, z_i). Then, the residual of this point is expressed as:

$$\delta_i = \left| \sqrt{(x_i - x_0)^2 + (y_i - y_0)^2 + (z_i - z_0)^2} - R \right| \tag{9}$$

The *RMS* is defined as the square root of the mean of the squared residuals of all points:

$$RMS = \sqrt{\frac{1}{N} \sum_{i=1}^{N} \delta_i^2} \tag{10}$$

where N is the total number of point cloud points. A smaller *RMS* value indicates that the fitted sphere more closely matches the point cloud data, corresponding to higher fitting accuracy.

The calculation results indicate that the *RMS* values of the three calibration spheres are as follows:

$$Sphere1 : RMS = 0.0078 \text{ mm} \tag{11}$$

$$Sphere1 : RMS = 0.0075 \text{ mm} \tag{12}$$

$$Sphere1 : RMS = 0.0079 \text{ mm} \tag{13}$$

The RMS of each sphere is less than 0.1 mm, indicating satisfactory fitting and stitching accuracy. The values of Sphere 2 and Sphere 3 are similar, suggesting a relatively uniform distribution of point cloud data for these two spheres. The RMS value of Sphere 1 is slightly higher, which may be attributed to an oblique scanning angle or partial surface occlusion.

To further illustrate the characteristics of residual distribution, the Z-direction residual distribution plots of the three fitted spheres are presented in Figure 13. It can be observed that the residuals are mainly concentrated within the range of ±0.05 mm, with local extreme

values not exceeding ±0.1 mm. The overall distribution appears symmetric, indicating that the model does not exhibit systematic deviation.

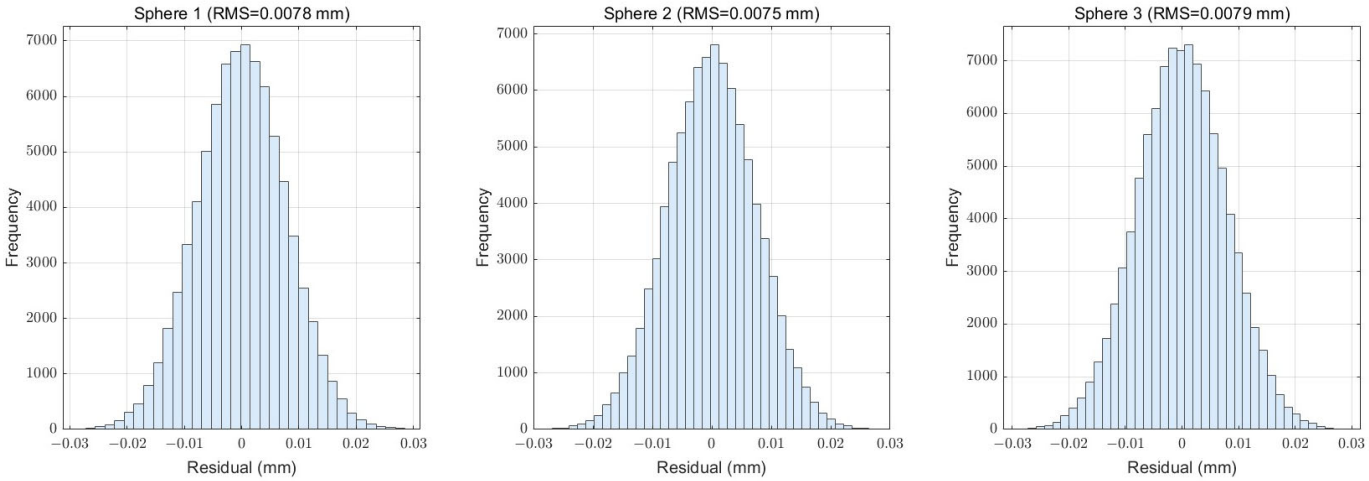


Figure 13. Residual distribution of three fitted spheres along the Z-direction.

In summary, the *RMS* errors of the three spheres are all controlled within 0.1 mm, satisfying the accuracy requirements of system calibration. The primary error sources include variations in scanning angle, differences in surface reflectivity, and sparsity of edge points. Overall, the calibration and stitching model can accurately reconstruct the geometric characteristics of standard spheres, providing a stable reference for subsequent nozzle hole measurement and 3D reconstruction.

3.3. Data Stitching

Through calibration of the measurement system, the homogeneous transformation matrices M_L and M_R of the two line laser sensors in the camera coordinate system are obtained, which define the spatial correspondence between each sensor coordinate system and the world coordinate system and support the implementation of data stitching, a process that integrates multi-view point clouds into a unified global coordinate frame. By applying these transformation matrices to the nozzle hole point cloud data acquired by the left and right line laser sensors, the spatial unification and stitching of multi-view point clouds can be achieved. Let the nozzle hole point cloud data collected by the left and right sensors be L_P and R_P, respectively, and their corresponding coordinates in the world coordinate system be W_LP and W_RP, respectively. According to the principle of homogeneous transformation, the two can be expressed as:

$$W_L p = M_L L_P \tag{14}$$

$$W_R p = M_R R_P \tag{15}$$

By transforming the point clouds into the same coordinate system, the stitching of the nozzle hole point cloud can be completed. As illustrated in Figure 14, the stitched nozzle hole point cloud achieves accurate spatial overlap, with continuous boundaries between the left and right fields of view and smooth transitions, indicating that the calibration accuracy satisfies the requirements for high-precision geometric reconstruction. Since the aperture of the nozzle hole is only about 2 mm, it is difficult to directly identify the orifice edge in the overall stitched point cloud. Therefore, it is necessary to further extract local regions for feature analysis in subsequent processing.

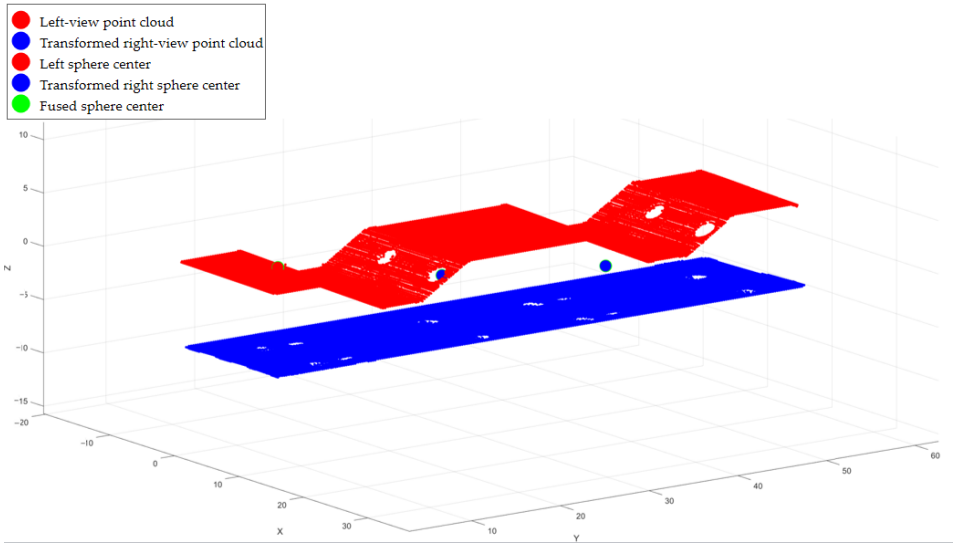


Figure 14. Stitching result of the nozzle orifice point cloud.

4. Data Processing and Experimental Verification

Further processing is performed on the stitched point cloud data to determine the aperture and center coordinates of the nozzle hole, thereby obtaining the impingement accuracy of paired nozzle holes. Subsequently, multiple sets of experiments are conducted to verify the robustness of the algorithm, so as to further improve measurement accuracy and efficiency.

4.1. Aperture Measurement

The processing flow of the nozzle orifice point cloud data is illustrated in Figure 15.

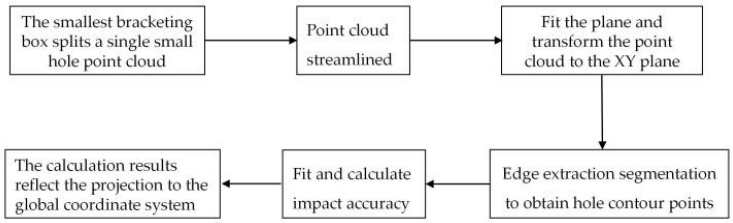
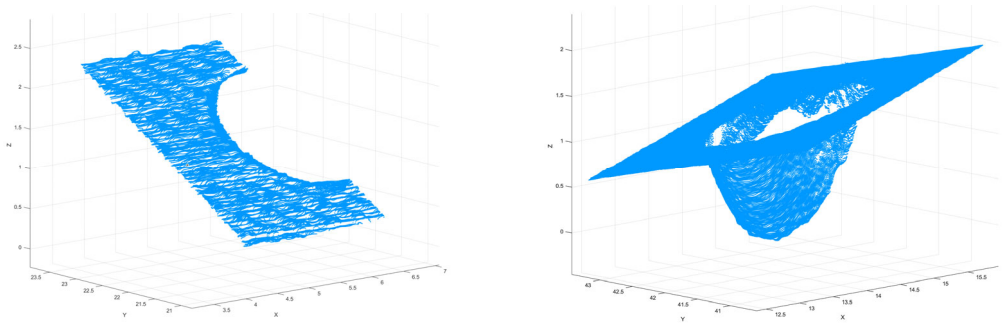


Figure 15. Data processing flow of the nozzle orifice.

First, the smallest bounding box method is applied to segment the region containing the nozzle orifice and its surrounding data within the point cloud. After segmentation, the point cloud size of a single nozzle orifice is about 3 mm × 3 mm. To enhance the efficiency and accuracy of data processing, the segmented nozzle orifice point cloud is simplified through operations such as downsampling and radius filtering.

When measuring micro-hole diameters using orifice point cloud data, as shown in Figure 16a, there are significant inherent errors. In addition, the measurement results are easily affected by orifice chamfers, as shown in Figure 16b. Differences in the chamfer precision of small holes also lead to distinct deviations. To address these issues and improve the accuracy and consistency of nozzle orifice parameter measurement, this paper proposes an enhanced 3D point cloud data processing method. To reduce potential distortion caused by single 2D projection, a robust plane fitting algorithm with automatic outlier elimination is adopted to accurately calculate the normal vector of the local plane. Instead of projecting all points onto a single plane, multiple cross-sectional point clouds at different shallow depths near the orifice entrance are extracted and fitted individually, and the average value

of these fitting results is taken as the final aperture. According to verification, within the machining accuracy of actual engineering orifices, the deviation caused by slight taper or ellipticity is quite small, and the proposed method can still achieve reliable and stable measurement results. This optimization effectively suppresses projection distortion and further improves the accuracy and robustness of aperture measurement. When collecting the micro-hole point cloud, partial data of the hole wall are included. By adjusting the measurement angle of the object, point cloud data from different regions of the hole inner wall can be obtained and uniformly transformed to the plane where the small hole is located, so that the end-face data of the small hole can accurately represent the diameter measurement results.



(**a**) (**b**)

Figure 16. Schematic diagram of the nozzle orifice structure: (**a**) Orifice chamfer point cloud; (**b**) Partial inner wall point cloud.

The specific steps are as follows: First, least-squares fitting is performed on the simplified point cloud plane to determine the plane pose of the point cloud. Then, this plane pose is converted into a homogeneous matrix, and its inverse matrix is calculated and applied to the nozzle orifice point cloud, transforming the hole plane to the XY plane. Finally, all points are projected onto the XY plane to obtain a clear and complete micro-hole point cloud, as shown in Figure 17.

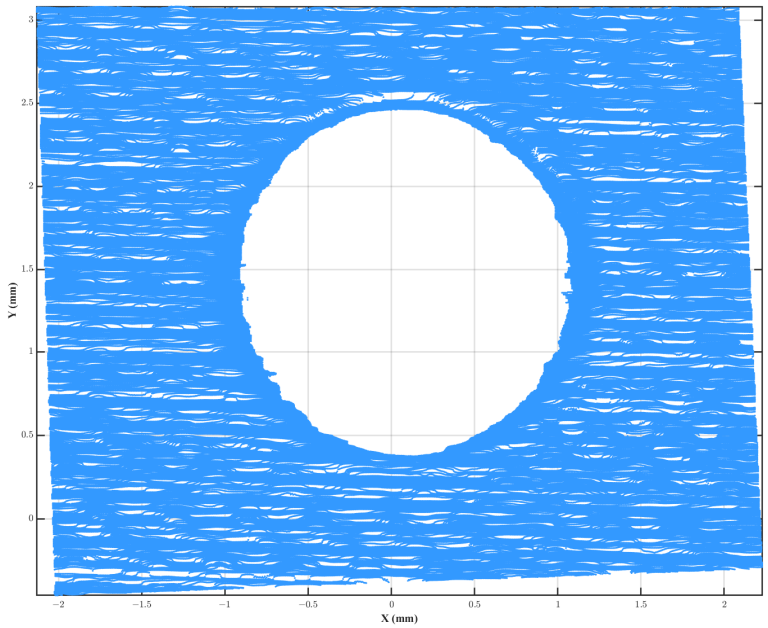
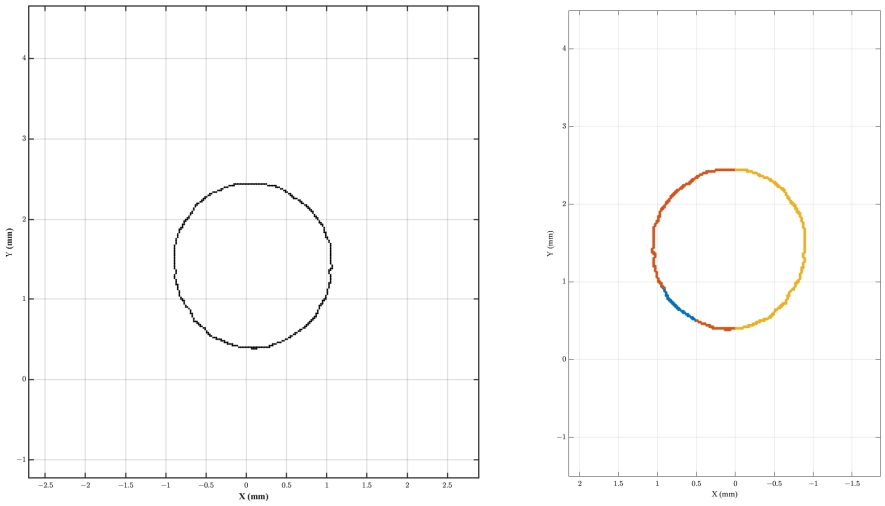


Figure 17. Point cloud transformed to the XY plane.

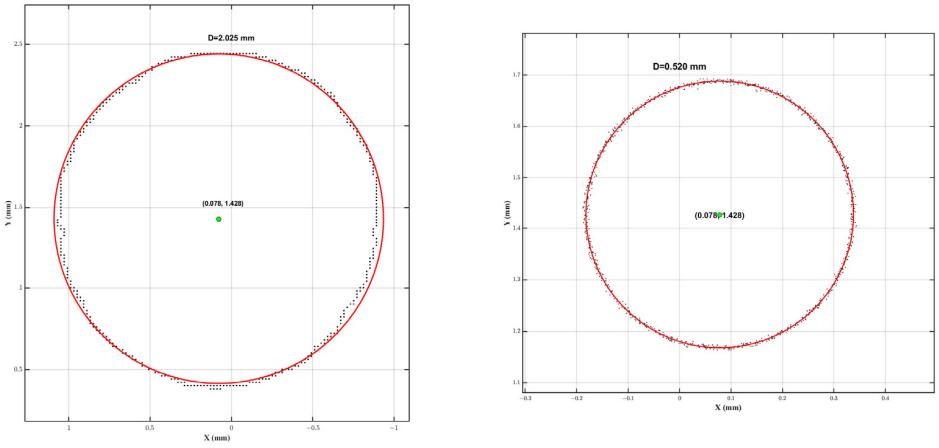
After obtaining the two-dimensional point cloud, the α-shape algorithm is employed to extract the 2D boundary points of the micro-holes. As shown in Figure 18a, the algorithm achieves effective extraction of the plane and circular hole edges, which are complete and well-defined. Subsequently, the K-means clustering method is applied to segment the boundary points. Considering that K-means is sensitive to point cloud noise and irregular chamfer geometries common in mass-drilled injector plates, we first perform outlier elimination preprocessing to suppress scattered noise and set reasonable initial clustering parameters based on the structural prior of the orifice chamfer. These optimizations ensure stable and accurate segmentation of the plane boundary and hole boundary, as illustrated in Figure 18b.



(**a**) (**b**)

Figure 18. Extraction of micro-hole contour points: (**a**) Edge extraction; (**b**) Clustering segmentation.

Finally, based on the extracted micro-hole edge data, the indirect adjustment method is used for fitting. The fitting results of two representative micro-hole contours are presented in Figure 19, with the 2.0 mm diameter hole shown in Figure 19a and the 0.5 mm diameter hole shown in Figure 19b. These two examples demonstrate the adaptability of the proposed method to different aperture sizes. Since the parameters obtained from fitting are measured after projection, they need to be transformed back into the world coordinate system.



(**a**) (**b**)

Figure 19. Fitting of hole contour points: (**a**) Φ2 mm hole; (**b**) Φ0.5 mm hole.

4.1.1. Comparison with the 2.0 mm Diameter Hole

The aperture of each nozzle hole in the point cloud data is measured sequentially. To verify the accuracy of the proposed aperture measurement method, the Aoying AX3000 microfocus industrial CT (Aoying Testing Technology (Shanghai) Co., Ltd., Shanghai, China) is employed to perform comparative measurements on the test specimen, and the scanning result is shown in Figure 20. Industrial CT can obtain internal structural information of the workpiece under non-contact conditions, extract the two-dimensional boundary point set of the nozzle hole through cross-sectional profile extraction, and then apply least-squares circle fitting to calculate the aperture.

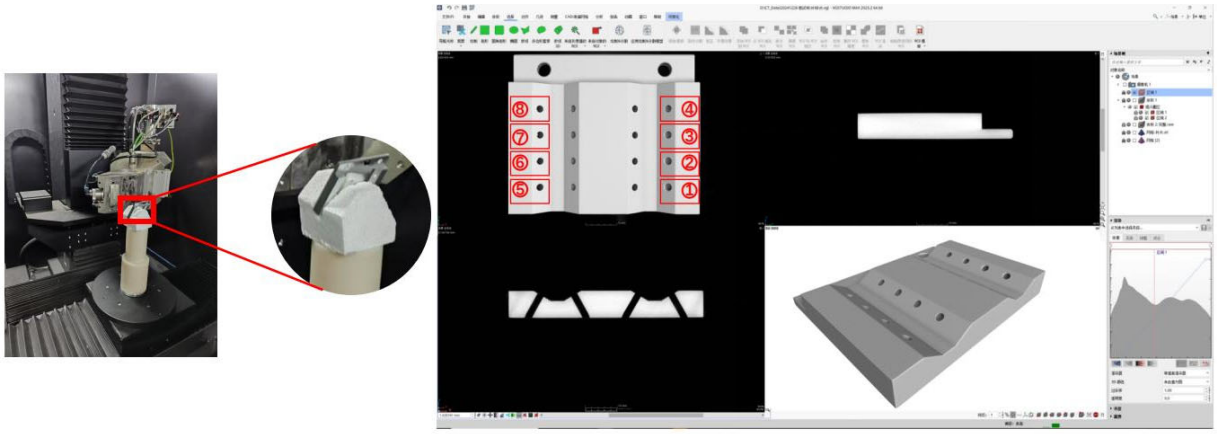


Figure 20. Industrial CT scanning results.

Based on the industrial CT scanning results, the two-dimensional cross-section contours corresponding to each nozzle hole are extracted, and the aperture is calculated using the least-squares circle fitting method, as shown in Figure 21.

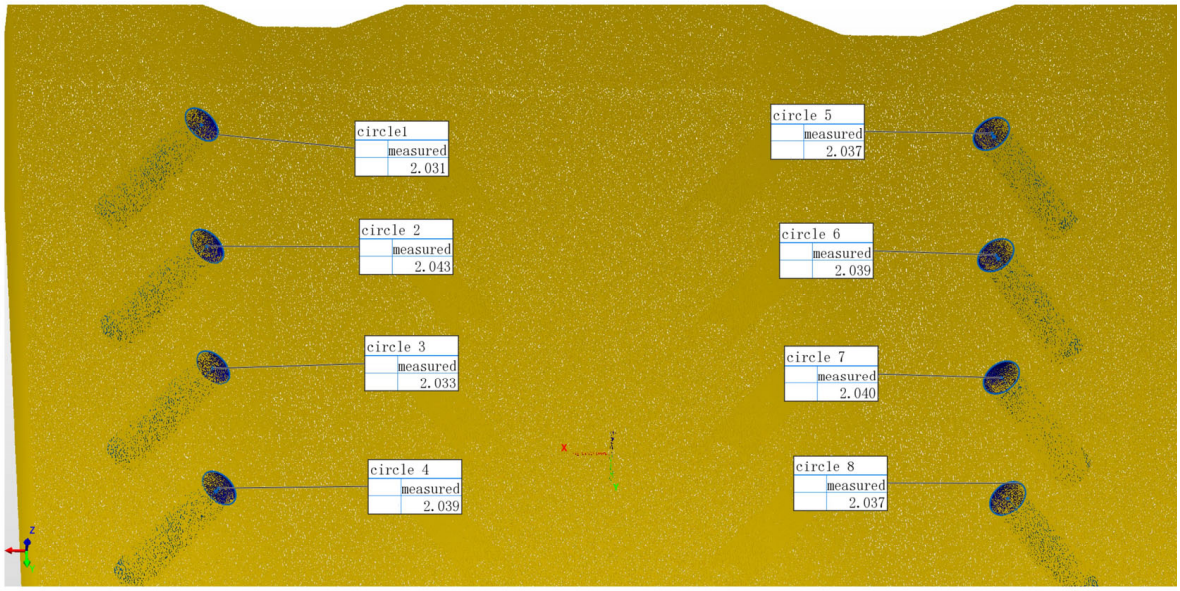


Figure 21. Aperture from industrial CT scanning.

To verify the accuracy of the proposed method, 8 nozzle holes are selected and measured using both the dual-line laser method and the industrial CT method. The comparison results are presented in Table 1.

Table 1. Comparison results between dual-line laser and industrial CT.

Hole No.	Dual-Line Laser Method/mm	Industrial CT/mm	Absolute Deviation/mm	Absolute Deviation/μm	Relative Error/%
1	Φ2.025	Φ2.031	0.006	6	0.30
2	Φ2.021	Φ2.043	0.022	22	1.09
3	Φ2.022	Φ2.033	0.011	11	0.54
4	Φ2.023	Φ2.039	0.016	16	0.79
5	Φ2.020	Φ2.037	0.017	17	0.84
6	Φ2.026	Φ2.039	0.013	13	0.64
7	Φ2.023	Φ2.040	0.017	17	0.84
8	Φ2.019	Φ2.037	0.018	18	0.89

4.1.2. Comparison with the 0.5 mm Diameter Hole

For the 0.5 mm diameter micro-hole, a Gocator 4000 series 3D coaxial line confocal sensor (LMI Technologies Inc., Burnaby, BC, Canada) is used to perform high-precision comparative measurements. This sensor enables non-contact, high-resolution 3D scanning without shadow interference, and is capable of capturing high-precision point cloud data of the micro-hole contour. The two-dimensional boundary point set of the nozzle hole is extracted through cross-sectional profile processing, and the least-squares circle fitting method is applied to calculate the aperture. The scanning and fitting results are shown in Figure 22.



Figure 22. Scanning result obtained by the 3D intelligent line confocal sensor.

The aperture measurement is carried out using the proprietary self-developed software of this sensor, as illustrated in Figure 23.

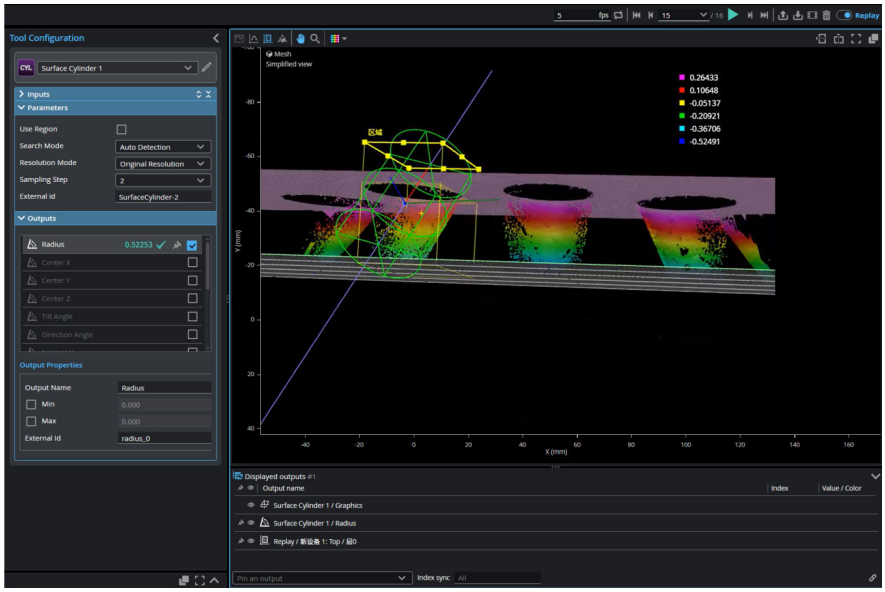


Figure 23. Diameter detection results obtained by the 3D intelligent line confocal sensor.

The comparison results are presented in Table 2.

Table 2. Comparison results between dual-line laser and 3D intelligent line confocal sensor.

Hole No.	Dual-Line Laser Method/mm	3D Intelligent Line Confocal Sensor/mm	Absolute Deviation/mm	Absolute Deviation/μm	Relative Error/%
1	Φ0.520	Φ0.531	0.011	11	2.07
2	Φ0.512	Φ0.523	0.011	11	2.10
3	Φ0.514	Φ0.522	0.008	8	1.53
4	Φ0.526	Φ0.539	0.013	13	2.41
5	Φ0.518	Φ0.530	0.012	12	2.26
6	Φ0.515	Φ0.522	0.007	7	1.34

In this study, the accuracy of the proposed dual-line laser method was validated through two sets of experiments on different-sized nozzle holes.

For the 2.0 mm nozzle holes, the measurement results obtained by high-precision industrial CT were taken as the reference standard. As shown in Table 1, the proposed method achieved good agreement with the CT results. For the 8 tested holes, the maximum absolute deviation was 0.022 mm (22 μm), the average absolute deviation was 0.015 mm (15 μm), the maximum relative error was 1.09%, and the average relative error was 0.74%.

To further evaluate the method's performance on smaller-sized holes, additional validation was conducted on 0.5 mm micro-holes, using the 3D intelligent line confocal sensor as the reference. As shown in Table 2, while the overall trend remains consistent, the errors for the 0.5 mm holes are slightly larger: the maximum absolute deviation reaches 0.013 mm (13 μm), with an average absolute deviation of approximately 0.010 mm (10 μm); the maximum relative error is 2.41%, and the average relative error is 1.95%.

The slightly higher relative error for the 0.5 mm holes is primarily due to the smaller feature size. At this scale, minor machining imperfections, edge rounding, and boundary detection noise have a proportionally larger impact on the measured diameter, making accurate measurement inherently more challenging.

Considering these factors, the results demonstrate that the proposed method maintains good consistency with different reference standards across both 2.0 mm and 0.5 mm apertures, confirming its effectiveness and reliability for nozzle hole diameter measurement.

It should be noted that all methods adopt the least-squares circle fitting criterion, but differ in raw data acquisition: the proposed method uses dual-line laser scanning, while industrial CT and the confocal sensor use volumetric reconstruction and high-precision profile scanning, respectively. A unified fitting strategy was adopted to ensure comparability, emphasizing the consistency of aperture results across different measurement approaches.

4.2. Stagger Measurement

4.2.1. Comparison with the 2.0 mm Diameter Hole

Circle fitting is performed on the orifice contours on both sides of the 8 pairs of stitched nozzle holes, resulting in four orifice circles and their corresponding center coordinates. The normal vector of the fitted local inclined plane where the orifice is located is utilized to spatially constrain the circle fitting results, thereby improving the stability of orifice feature extraction. For the same nozzle hole, the corresponding orifice circle centers on both sides jointly define the spatial axis of the hole, based on which the axes of the paired nozzle holes can be established. The spatial included angle between the two axes is then calculated, and combined with their spatial intersection relationship as shown in Figure 24, the nozzle hole stagger angle and the position of the theoretical intersection point can be determined. Using this method, the spatial stagger of the eight pairs of nozzle holes can be obtained.

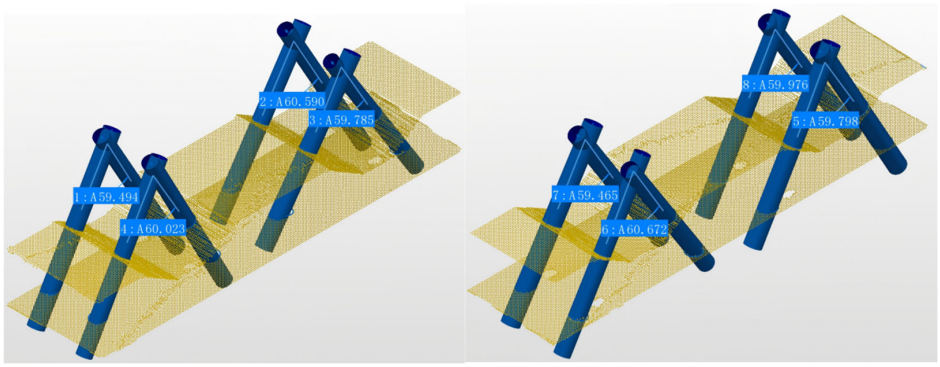


Figure 24. Spatial intersection of 2 mm nozzle holes.

To validate the accuracy of the proposed stagger angle measurement method, a pin gauge-assisted coordinate measuring approach is employed for comparative measurement on the test specimen, as shown in Figure 25. This method is implemented based on the Hexagon H3C-T300W coordinate measuring machine. The specific procedure is as follows: The theoretical machining diameter of the nozzle holes is Φ2 mm, although machining errors are present in actual production. Slender pin gauges with diameters ranging from 1.91 mm to 2.30 mm are selected, with a diameter interval of 0.01 mm for each specification. After determining the best-matched pin gauge through trial insertion, it is inserted into each pair of nozzle holes to be measured, so that the axis of the pin gauge about represents the axis direction of the nozzle hole.

Subsequently, 20 non-coplanar spatial discrete point coordinates are collected on the surface of each pin gauge using a coordinate measuring machine. The measurement data are imported into MATLAB, and the least-squares method is applied to perform spatial straight-line fitting on the two sets of discrete points, obtaining the corresponding direction vectors as shown in Figure 26, where panels 1–8 correspond to the eight pairs of nozzle holes listed in Table 3. Let the two direction vectors be μ and υ, respectively, then the stagger angle θ of the nozzle holes can be expressed as:

$$\theta = \arccos\left(\frac{\mu \cdot \nu}{\|\mu\|\|v\|}\right) \tag{16}$$

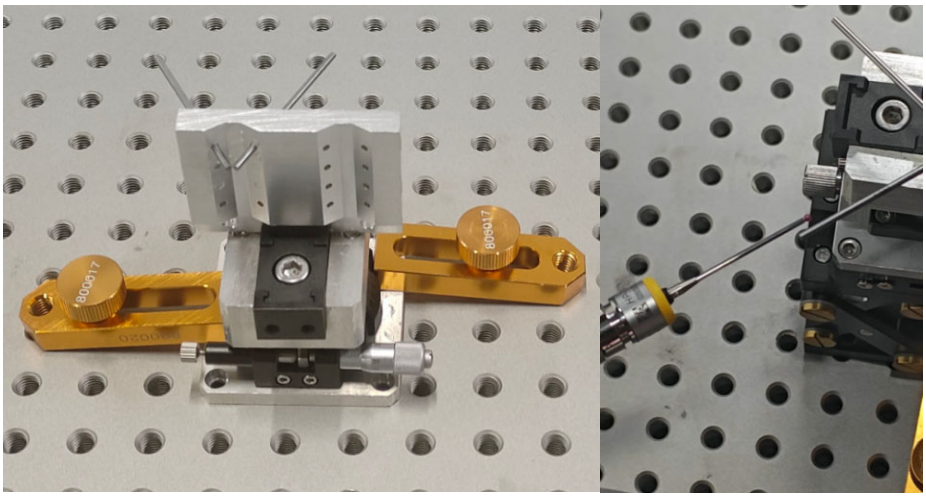


Figure 25. Isometric view of pin gauge and small hole assembly.

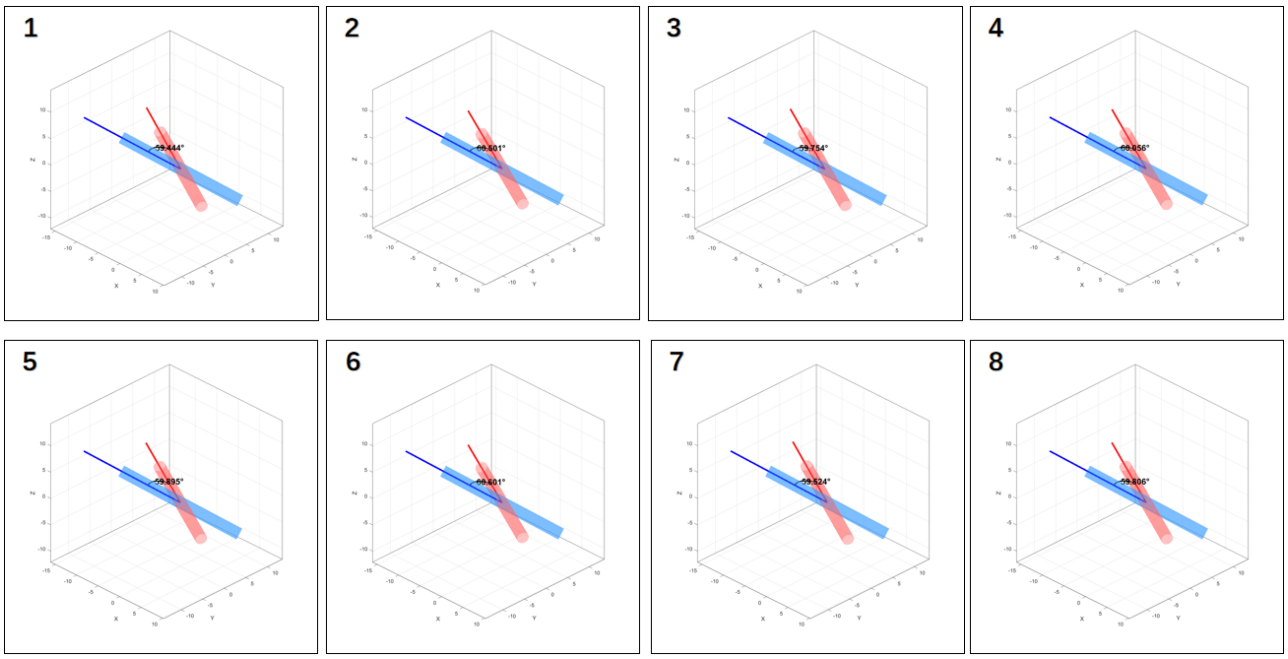


Figure 26. Angle calculation by CMM method.

Table 3. Comparison of nozzle hole stagger angles measured by the proposed method and CMM.

Hole No.	Dual-Line Laser Method/°	CMM + Pin Gauge Method/°	Absolute Deviation/°	Relative Error/%
1	59.494	59.444	0.050	0.084
2	60.590	60.501	0.089	0.147
3	59.785	59.754	0.031	0.052
4	60.023	60.056	−0.033	−0.055
5	59.798	59.895	−0.097	−0.162
6	60.672	60.601	0.071	0.117
7	59.465	59.524	−0.059	−0.099
8	59.976	59.806	0.170	0.284

μ and v are the direction vectors of the two paired orifices.

To further verify the accuracy of the proposed method, 8 pairs of nozzle holes are selected and measured using both the proposed method and the pin gauge-assisted CMM method. The comparison results are shown in Table 3.

4.2.2. Comparison with the 0.5 mm Diameter Hole

For the 0.5 mm holes, the same method is applied to calculate the spatial intersection degree, as presented in Figure 27.The yellow part represents point cloud data and the blue part denotes the fitted aperture.

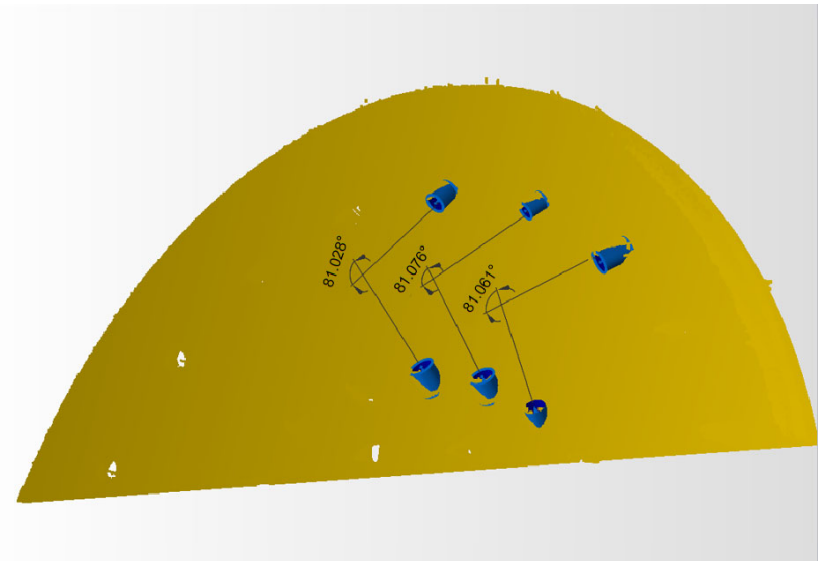


Figure 27. Spatial intersection of 0.5 mm nozzle holes.

Similarly, the proprietary software of the Gocator 4000 series 3D coaxial line confocal sensor is used to verify the spatial stagger. Due to the relatively large errors caused by the machining process, three pairs of well-machined nozzle holes are selected for verification. The results are shown in Figure 28.

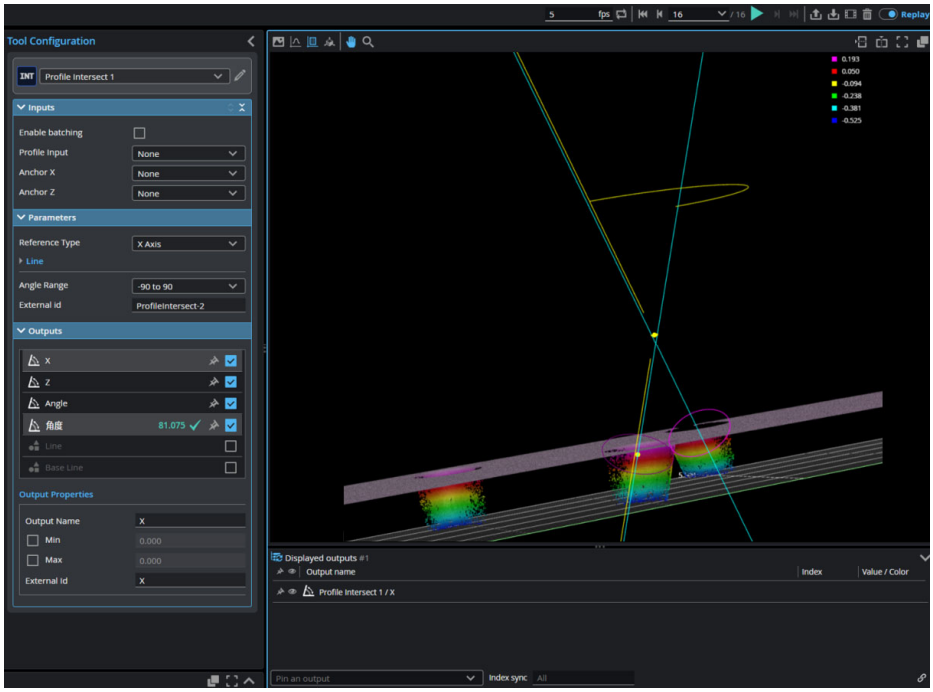


Figure 28. Intersection angle detection results obtained by the 3D intelligent line confocal sensor.

The comparison results between the Gocator 4000 series 3D coaxial line confocal sensor and the dual-line laser method are shown in Table 4.

Table 4. Comparison of nozzle hole stagger angles between the proposed method and 3D coaxial line confocal sensor.

Hole No.	Dual-Line Laser Method/°	3D Intelligent Line Confocal Sensor/mm	Absolute Deviation/°	Relative Error/%
1	81.028	81.075	0.047	0.058
2	81.076	81.088	0.012	0.015
3	81.061	81.105	0.044	0.054

For the nozzle hole stagger angle (alignment deviation) evaluation, the measurement results obtained by the pin gauge-assisted CMM method are taken as the true reference values for the 2.0 mm nozzle holes. It can be seen from Table 3 that the nozzle hole stagger angles measured by the proposed method and the pin gauge-assisted CMM method exhibit a consistent overall variation trend. For the 8 pairs of nozzle holes, the maximum absolute deviation is 0.170°, and the average absolute deviation is 0.076°; the maximum relative error is 0.284%, and the average relative error is 0.125%. Considering the influence of factors such as pin gauge assembly clearance, CMM sampling error, and point cloud fitting error, slight deviations still exist between the two methods; however, the overall consistency remains good, which confirms the effectiveness and reliability of the proposed method in measuring nozzle hole stagger angles.

To further validate the performance of the proposed method on smaller-sized holes, additional experiments were conducted on 0.5 mm micro-holes, using a 3D intelligent line confocal sensor as the reference standard. As shown in Table 4, the stagger angle results measured by the proposed method show good agreement with those obtained by the confocal sensor. The maximum absolute deviation is 0.047°, and the maximum relative error is only 0.058%, further verifying the accuracy of the method for micro-hole alignment deviation measurement.

To verify the comprehensive measurement efficiency, the total scanning time of the proposed dual-line laser method is only 10 s, and the overall data processing time for both aperture and alignment deviation is 10 min. In comparison, industrial CT requires 30 min for scanning and 5 min for data processing only to obtain the aperture measurement result, while the CMM with pin gauges needs 30 min for pin gauge selection and sampling and another 30 min for cylinder axis fitting and stagger angle calculation only for alignment deviation measurement. The 3D intelligent line confocal sensor requires only 3 min for scanning and 20 min for data processing, but its equipment cost is significantly higher than that of the proposed system. The proposed method can realize simultaneous measurement of aperture and alignment deviation in a single process, showing significant efficiency advantages over traditional methods, while maintaining a much lower equipment cost compared to high-end confocal sensors.

5. Conclusions

This paper investigates a measurement method for the micro-orifice diameter and impingement accuracy of unlike impinging injectors, and the following conclusions are drawn:

(1) Based on the laser triangulation principle, the edge features of micro-holes can be effectively captured using a line laser sensor combined with high-precision motion control. The geometric shape of micro-holes can be fully reconstructed through accurate data stitching and processing, which demonstrates the feasibility of the measurement principle.

(2) The use of a high-resolution line laser sensor enables the acquisition of fine features at the edge of both 2 mm and 0.5 mm nozzle holes, ensuring sufficient data density and

measurement accuracy for conventional orifices and micro-holes. The total scanning time is only 10 s, and the overall data processing time for both aperture and alignment deviation is 10 min, which is much faster than industrial CT, CMM and 3D coaxial line confocal sensor. The non-contact rapid scanning ensures high measurement efficiency for nozzle holes with different diameters, meeting the requirements of both high precision and high efficiency.

(3) Through high-precision point cloud data and mathematical fitting models, the position of the virtual impingement point can be accurately quantified, providing key indicators for evaluating the impingement accuracy of nozzle holes.

(4) This study proposes a novel measurement approach for nozzle holes, achieving high-precision and high-efficiency measurement of micro-orifice diameter and impingement accuracy in injectors. This method provides a more practical and reliable technical solution for the field of micro-hole precision manufacturing, with significant application potential.

Author Contributions: Conceptualization, H.L., Y.B. and L.Y.; methodology, H.L.; software, Y.W., Y.B. and C.M.; validation, Y.B. and M.Z.; data curation, Y.B. and Y.W.; writing—original draft preparation, H.L., Y.B. and Y.Z.; writing—review and editing, H.L. and J.L.; All authors have read and agreed to the published version of the manuscript.

Funding: This work was supported by the Shaanxi Province Qinchuangyuan "Scientist + Engineer" Team Building (2024QCY-KXJ-006), the Shaanxi Provincial Department of Education Local Service Special Project (Industrialization Cultivation Project) (24JC007), the Shaanxi Provincial Office of Science, Technology and Industry for National Defense "Open Competition" Project (2024SXGB008), the Xian New Area Science and Technology Plan Project Key R&D Project (XJZZ-2023-009).

Data Availability Statement: The data presented in this study are available on request from the corresponding author.

Conflicts of Interest: The authors declare no conflicts of interest.

Abbreviations

The following abbreviations are used in this manuscript:

CT	Computed Tomography
CMM	Coordinate Measuring Machine
ICP	Iterative Closest Point
RMS	Root Mean Square

References

1. Martin, D.; Brooks, M.; Pitot, J.; Cooper, R.; Wunderlin, N. A structured approach to the design and testing of LOX/kerosene impinging-jet injectors. *Aerosp. Sci. Technol.* **2026**, *168*, 111095. [CrossRef]
2. Wang, K.; Shen, C.; Fan, B. Effect of Injector recess depth on flame structure of single injector in air heater. *Aerospace* **2026**, *13*, 21. [CrossRef]
3. Pai, R.; Lokesh, K.; Mayya, D.S.; Vidyashree, H.; Yallappa, R.; Jayashree, J.; Neha, K.; Sagar, K. Analysis of design parameters of fuel injector used in liquid propellant rocket engine. *Mater. Today Proc.* **2023**, *92*, 344–355. [CrossRef]
4. Small, J.C.; Zhang, L. Computational study of fluidic-valve injectors for detonation engines. *Aerospace* **2024**, *11*, 171. [CrossRef]
5. Liu, Q.; Li, P.; Sun, H.; Zhang, D.; Ji, B.; Yang, L.; Fu, Q. Spray characteristics of gel containing nanoparticles in impinging jet injectors. *Acta Astronaut.* **2025**, *232*, 94–102. [CrossRef]
6. Broniarz-Press, L.; Włodarczak, S.; Matuszak, M.; Ochowiak, M.; Idziak, R.; Sobiech, Ł.; Szulc, T.; Skrzypczak, G. The effect of orifice shape and the injection pressure on enhancement of the atomization process for pressure-swirl atomizers. *Crop Prot.* **2016**, *82*, 65–74. [CrossRef]
7. Zhang, C.; Zhang, Z.; Wu, K.; Xia, X.; Fan, X. Atomization of misaligned impinging liquid jets. *Phys. Fluids* **2021**, *33*, 093311. [CrossRef]

8. Stone, J.; Muralikrishnan, B.; Sahay, C. Geometric effects when measuring small holes with micro contact probes. *J. Res. Natl. Inst. Stand. Technol.* **2011**, *116*, 573–587. [CrossRef]
9. Liu, Y.; Ding, K.; Birnbaum, A.J.; Rawlings, A.; Sun, A.; Chen, W.; McDowell, D.L.; Michopoulos, J.G.; Zhu, T. Surface plasticity in laser scanning of metals. *Acta Mater.* **2026**, *302*, 121667. [CrossRef]
10. Qiu, Z.; Tang, J. Three-dimensional information measurement and reconstruction for micro-hole array based on the modified shape from focus. *Opt. Lasers Eng.* **2024**, *178*, 108246. [CrossRef]
11. Sun, Y.; Shi, Z.; Yu, B.; Li, H. Incident angle model of measuring light in gear measurement utilizing a line laser sensor and analysis on its influence factors. *Measurement* **2022**, *203*, 111838. [CrossRef]
12. Herl, G.; Wittl, S.; Jung, A.; Handke, N.; Weiss, A.; Eberhorn, M.; Oeckl, S.; Zabler, S. RoboCT: The state and current challenges of industrial twin robotic CT systems. *Sensors* **2025**, *25*, 3076. [CrossRef] [PubMed]
13. Wang, L.; Xu, Y.; Li, Q.; Gao, L.; Xu, Y. Optimization scheme of measuring accuracy of bearing seat size based on machine vision. *Int. J. Comput. Sci. Inf. Technol.* **2024**, *2*, 223–235. [CrossRef]
14. Rivera-Ortega, U. Using a machine vision sensor for wavelength estimation by measuring an Airy disk, with didactic purposes. *Phys. Educ.* **2024**, *59*, 015034. [CrossRef]
15. Wang, T.; Liu, Y.; Zhang, W.; Lei, Y.; Lin, J.; Fu, H.; Lin, Z. The research for quickly measuring the diameter and roundness of solder balls based on machine vision technology. *J. Electron. Packag.* **2024**, *146*, 10. [CrossRef]
16. Zhang, K.; Wang, C.; Li, Q.; Wang, Z. Characterization of the nozzle ablation rate based on 3D laser scanning system. *Aerospace* **2023**, *10*, 172. [CrossRef]
17. Zhang, M.; Yan, X.-S.; Xi, X.-C.; Zhao, W.-S. Measurement of axial orientation of film cooling holes based on a laser sensor. *Procedia CIRP* **2022**, *113*, 172–177. [CrossRef]
18. Liu, Y.; Yu, D.; Du, H.; Chen, T. Measurement of form and position error of small-diameter deep holes based on collaboration between a lateral confocal displacement sensor and helical scanning. *Sensors* **2025**, *25*, 6863. [CrossRef]
19. Plaza, S. Improving the efficiency and quality of sustainable industrial CT by optimizing scanning parameters. *Sensors* **2025**, *25*, 2440. [CrossRef]
20. Zhagn, B.; Jiang, Y.; Wu, Q.; Zhang, Q. Three-dimensional shape measurement method and system calibration for an annular Inner-wall. *Opt. Express* **2025**, *33*, 3670–3684. [CrossRef]
21. He, Q.; Ji, Z.; Li, Q.; Liu, X. A 3D calibration method for binocular vision system. *Meas. Sci. Technol.* **2025**, *36*, 015218. [CrossRef]
22. Lian, D.; Yang, R.; Guo, M.; Gao, S.; Huang, J.; Li, J.; Liu, Y.; Tan, J. Telecentric imaging-based dimensional measurement for rotational components with magnification and edge localization error correction. *IEEE Trans. Instrum. Meas.* **2025**, *74*, 5045309. [CrossRef]
23. Kabsch, W. A solution for the best rotation to relate two sets of vectors. *Acta Cryst. A* **1976**, *32*, 922–923. [CrossRef]
24. Besl, P.J.; McKay, N.D. A method for registration of 3-D shapes. *IEEE Trans. Pattern Anal. Mach. Intell.* **1992**, *14*, 239–256. [CrossRef]

Disclaimer/Publisher's Note: The statements, opinions and data contained in all publications are solely those of the individual author(s) and contributor(s) and not of MDPI and/or the editor(s). MDPI and/or the editor(s) disclaim responsibility for any injury to people or property resulting from any ideas, methods, instructions or products referred to in the content.